Enhanced oxygen evolution and zinc-air battery performance via electronic spin modulation in heterostructured catalysts

Linlin Yang, Ren He, Marc Botifoll, Yongcai Zhang, Yang Ding, Chong Di, ChuanSheng He, Ying Xu, Jordi Arbiol, Yingtang Zhou, and Andreu Cabot**

Linlin Yang, Ren He, Andreu Cabot*
Catalonia Energy Research Institute – IREC, Sant Adrià de Besòs, 08930, Barcelona, Catalonia, Spain
E-mail: acabot@irec.cat

Linlin Yang, Ren He
Enginyeria Electrònica i Biomèdica Facultat de Física, Universitat de Barcelona, 08028, Barcelona, Spain

Marc Botifoll, Jordi Arbiol
Catalan Institute of Nanoscience and Nanotechnology (ICN2), CSIC, BIST, Campus UAB, Bellaterra, 08193, Catalonia, Spain

Yongcai Zhang
School of Chemistry and Chemical Engineering, Yangzhou University, Yangzhou 225009, China

Yang Ding, Chong Di, Ying Xu,
Hebei Key Lab of Optic-electronic Information and Materials, College of Physics Science and Technology, Hebei University, Baoding, 071002, China

Chuansheng He
School of Materials Science and Engineering, University of Jinan, Jinan 250022, China

Jordi Arbiol, Andreu Cabot
ICREA, Pg. Lluis Companys, 08010 Barcelona, Catalonia, Spain

Yingtang Zhou*
National Engineering Research Center for Marine Aquaculture, Marine Science and Technology College, Zhejiang Ocean University, Zhoushan, Zhejiang Province, 316004, China
E-mail: zhouyingtang@zjou.edu.cn

Keywords: electrocatalysis, heterostructure, surface reconstruction, spin polarization, oxygen evolution reaction, zinc-air battery

Abstract: Spin polarization is an effective strategy, often overlooked, to boost activity and selectivity in a range of catalytic reactions including the oxygen evolution reaction (OER). This spin polarization is frequently accomplished using external magnetic fields, which makes it impractical for real applications. Herein, spin polarization is accomplished by engineering Ni/$MnFe_2O_4$ heterojunctions, whose surface is reconstructed into NiOOH/MnFeOOH during OER. NiOOH/MnFeOOH shows a large magnetic moment and high spin state of Ni, which modulates the OH^- and O_2 adsorption energy and helps the spin alignment of oxygen intermediates. As a result, NiOOH/MnFeOOH electrocatalysts provide excellent OER performance with an overpotential of 261 mV at 10 mA/cm^2. Besides, we demonstrate rechargeable zinc-air batteries based on Ni/$MnFe_2O_4$ showing a high open circuit potential of 1.56 V and excellent stability for over 360 h and more than 1000 cycles. This outstanding performance is rationalized using density functional theory calculations, which show that the optimal spin state of both Ni active sites and oxygen intermediates facilitates spin-selected charge transport, optimizes the reaction kinetics, and decreases the energy barrier to the evolution of oxygen. This study provides insight into spin

polarization modulation by magnetic heterojunctions that allow adjusting both metal active sites and oxygen intermediates without an external magnetic field to boost the OER performance.

1. Introduction

Electrochemical energy storage and conversion devices play a crucial role in the development of sustainable, environmentally friendly, and efficient energy systems to meet the demands of modern society.[1] Among them, rechargeable zinc-air batteries (ZABs) have emerged as promising candidates owing to their high energy density, safety, and environmental friendliness.[2] However, ZABs are limited by the sluggish kinetics of the multiple electron-proton coupling processes involved in the oxygen evolution reaction (OER) that takes place at the air cathode during ZAB charging.[3] Therefore, the development of highly efficient, low-cost, and durable OER catalysts is crucial for the realization of high-performance ZABs, among other electrochemical technologies.[4]

While noble metals are the main electrocatalysts used to activate the oxygen redox reactions, first-row transition metals, such as Mn, Fe, Co, and Ni, and their corresponding oxides, hydroxides, and oxyhydroxides, offer advantages in terms of abundance and cost, while exhibiting comparable catalytic performances in alkaline solution.[5] This high performance is generally associated with the abundant 3d electrons that can modulate the adsorption of oxygen intermediates and boost the OER process.[6]

Adjusting architecture,[7] composition,[8] heterointerfaces,[9] and exposed crystal facets[10] are some of the most successful strategies for modulating the performance of OER catalysts. Among them, the design and engineering of heterojunctions with proper electronic interphase interaction is particularly effective.[11] Within heterojunctions, the formation of a space charge region with

two oppositely charged areas and a strong internal field alters the electron density of nearby surface atoms affecting surface adsorption and charge transfer to relevant species.[12] The combination of a metal and a metal oxide is particularly used as it capitalizes on the high conductivity of metals and the tunable energy band level of metal oxides to generate effective oxygen catalysts.[13] For example, Niu et. al reported a Co/MnO heterostructure with optimized adsorption energy for oxygen-containing intermediates.[14] Dong et. al introduced a Mott-Schottky heterojunction Cu nanodots/Fe_2O_3 nanoislands that promoted the electron transfer from the metallic Cu to the semiconducting Fe_2O_3, thus improving the adsorptions towards O_2 and OH^- species.[15] Liu et.al constructed Co/CoO/nitrogen-doped reduced graphene oxide (N-rGO) and Ni/NiO/N-rGO, showing excellent OER performance related to the formed interfaces.[16]

In parallel, the control of the spin state of electrocatalytic surface sites has emerged as a key strategy to optimize catalytic performance, particularly for the OER.[17] In the OER, the paramagnetic triplet oxygen molecules, with two parallel aligned electrons in π^* orbitals, are formed from OH^-/H_2O with a diamagnetic singlet state with all electrons paired. Thus the kinetics of this reaction strongly depends on the spin state of electrocatalysts.[18] Inspired by this, several previous works have detailed the tuning of the spin state of the material to facilitate the combination of oxygen atoms with parallel spin arrangement. This spin manipulation has been usually accomplished through an external magnetic field.[19] However, applying an external magnetic field is not feasible in real-world devices.

As an alternative to the use of external magnetic fields, the regulation of electronic interactions between atoms, influencing atomic magnetic moments and spin polarization, holds the potential to be a viable approach for enhancing OER. In this direction, as an example, Sun et al. reported how charge transfer and catalytic behavior change with the different magnetic coupling

and corresponding spin moment/arrangement of one atom with its neighbors and probed the atomic spin moment of the active sites as a key indicator to predict the catalytic behavior.[20]

Herein, Ni/$MnFe_2O_4$ heterojunctions are produced to manipulate the electronic spin state at its surface. Then the performance of this heterojunction is evaluated as OER electrocatalysts. X-ray photoelectron spectroscopy (XPS), ultraviolet photoelectron spectroscopy (UPS), energy band level, in-situ Raman spectra analyses, and density functional theory (DFT) calculations are used to determine the effect of the heterojunction interphase and the spin modulation of both metal active sites and oxygen intermediates. Finally, ZABs based on these heterojunctions are produced and tested.

2. Results and Discussion.

$MnFe_2O_4$ nanoparticles were synthesized using a hydrothermal method followed by annealing (see details in the Experimental section within the Supporting Information, SI). Transmission electron microscopy (TEM) micrographs (Figure S1a) show the nanoparticles to be quasi-spherical and have an average size of 40 nm. High-resolution TEM (HRTEM) images and the corresponding indexed fast Fourier transform (FFT) power spectra reveal the cubic $MnFe_2O_4$ phase of the particles (Figure S1b, c). Besides, high-angle annular dark field (HAADF) scanning TEM (STEM) and electron energy loss spectroscopy (EELS) elemental maps display a uniform elemental distribution of Fe, Mn, and O within each nanoparticle (Figure S1d).

Ni nanoparticles were grown on the surface of $MnFe_2O_4$ through a simple impregnation process (see details in the SI). Briefly, proper amounts of the Ni precursor and $MnFe_2O_4$ were dissolved/suspended in deionized water through sonication. Then, the water was evaporated while continuously stirring the solution overnight at 90 ℃. The obtained dry powder was annealed at 550 ℃ for 3 h within a hydrogen atmosphere (Ar+5% H_2) to reduce the Ni^{2+} to Ni. Through the

annealing process, the nanoparticles maintained their morphology and size (**Figure 1a**). HRTEM analysis showed the presence of both the cubic $MnFe_2O_4$ phase (**Figure 1b**) and the Fm-3m crystal structure of metallic Ni (**Figure 1c).** X-ray diffraction (XRD) analysis confirmed the presence of both $MnFe_2O_4$ and Ni phases while discarding the presence of secondary crystalline phases (**Figure 1d**). A homogeneous distribution of the two phases, forming numerous heterojunctions, was observed by HAADF-STEM micrographs and EELS elemental maps (**Figure 1e**). **Figure 1g** shows a magnified Bragg-filtered image of the (111) planes from Ni and (113) planes from $MnFe_2O_4$ obtained from the red squared part of **Figure 1f**, displaying a heterojunction formed between a $MnFe_2O_4$ (green) and a Ni (red) crystal. The two crystal domains grow with a relative orientation that minimizes the geometrical stress down to 3% without forming a perfect epitaxy (see details in the Calculations section within SI). This relative orientation between the crystal planes of Ni and $MnFe_2O_4$ phases is frequently observed in the sample (Figure S2).

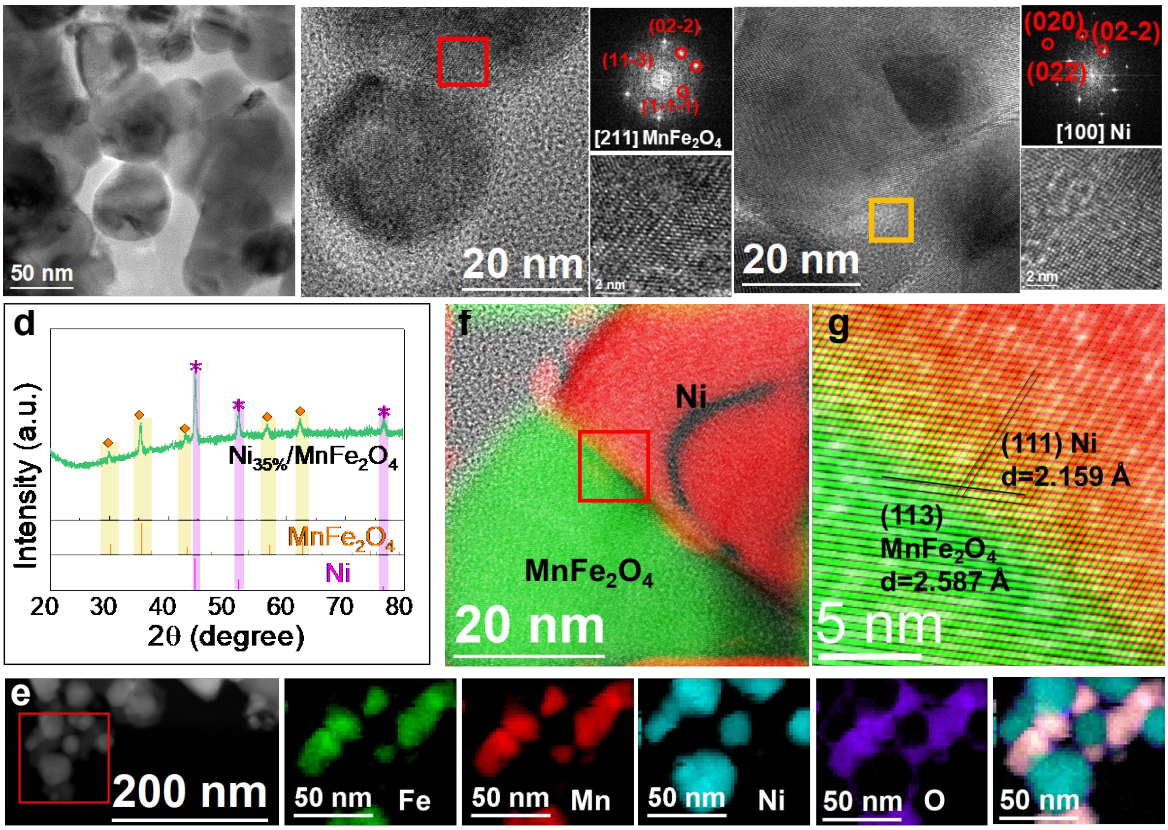

Figure 1. Material characterization of $Ni_{35\%}/MnFe_2O_4$ particles. (a) TEM image, (b-c) HRTEM images and its selected FFT patterns, and (d) XRD pattern with the reference pattern for $MnFe_2O_4$ (JCPDF No. 01-084-2781) and Ni (JCPDF No. 00-004-0850). (e) HAADF STEM micrograph and EELS elemental maps. (f, g) Bragg-filtered image of the (111) planes of Ni and (113) planes of $MnFe_2O_4$ at the $Ni_{35\%}/MnFe_2O_4$ interface. The yellow color arising at the interface and the black curved line in the Ni particle in panel f is an artifact generated by the delocalized signal of the Bragg-filtered (111) planes, typical of uncorrected electron microscopes.

Figure 2a shows the atomic composition as determined by energy-dispersive X-ray spectroscopy (EDS) and Figure S3 shows the XRD pattern of different $Ni/MnFe_2O_4$ samples produced with different Ni precursor amounts. The different samples are named $Ni_{x\%}/MnFe_2O_4$ where x% indicates the experimental Ni content measured.

The O 1s XPS spectra of $MnFe_2O_4$, $Ni_{35\%}/MnFe_2O_4$, and $Ni_{50\%}/MnFe_2O_4$ (**Figure 2b**) exhibit two peaks, assigned to lattice oxygen (O_L) and oxygen-containing surface species (O_s). $MnFe_2O_4$

shows the O_L peak position located at 529.96 eV. In the presence of Ni, this peak is blue-shifted to 530.11 eV ($Ni_{35\%}/MnFe_2O_4$) and 530.16 eV ($Ni_{50\%}/MnFe_2O_4$). The Fe 2p XPS spectrum of $MnFe_2O_4$ (**Figure 2c**) shows just one doublet at 710.37 eV (Fe $2p_{3/2}$), assigned to a Fe^{3+} chemical environment. The Fe 2p binding energy is also blue-shifted with the Ni loading to 710.54 eV for $Ni_{35\%}/MnFe_2O_4$ and 710.62 eV for $Ni_{50\%}/MnFe_2O_4$. The Mn 2p XPS spectrum of $MnFe_2O_4$ (**Figure 2d**) shows a doublet at 640.94 eV (Mn $2P_{3/2}$), assigned to Mn^{2+}. The Mn 2p binding energy was also positively shifted to 640.97 eV for $Ni_{35\%}/MnFe_2O_4$ and 641.28 eV for $Ni_{50\%}/MnFe_2O_4$. The simultaneous positive shift of the binding energies of O 1s, Fe 2p, and Mn 2p upon Ni loading indicates an upward shift of the Fermi level towards the conduction band, which is consistent with the injection of electrons from Ni to $MnFe_2O_4$. The Ni 2p XPS spectrum of $Ni_{35\%}/MnFe_2O_4$ (**Figure 2e**) exhibits two doublets at 852.85 and 855.61 eV (Ni $2p_{3/2}$) and the related satellite peaks, indicating the presence of Ni^0 and Ni^{2+} chemical environments. The Ni^{2+} is attributed to a slight oxidation of Ni during sample manipulation and transportation. The binding energies of the metallic component decrease to 852.66 eV with increasing Ni loading to $Ni_{50\%}/MnFe_2O_4$.

The electronic energy levels of $MnFe_2O_4$, $Ni_{35\%}/MnFe_2O_4$, and $Ni_{50\%}/MnFe_2O_4$ were further investigated using UPS (Figure S4). According to UPS spectra, the apparent work function of the $MnFe_2O_4$, $Ni_{10\%}/MnFe_2O_4$, $Ni_{20\%}/MnFe_2O_4$, $Ni_{35\%}/MnFe_2O_4$, and $Ni_{50\%}/MnFe_2O_4$ are 7.21, 6.88, 6.46, 6.31, and 6.04 eV, respectively (**Figure 2f**). This result denotes an upward Fermi level shift of $Ni/MnFe_2O_4$ with increased Ni loading, which is consistent with XPS data and the relatively lower work function of Ni (5.15 eV) compared with $MnFe_2O_4$.[21] The energy band diagram of Ni and $MnFe_2O_4$ is shown in **Figure 2g**. When Ni and $MnFe_2O_4$ form the heterojunction, electrons transfer from the low work function Ni to the larger work function $MnFe_2O_4$ to equilibrate the

Fermi levels. This charge redistribution generates a built-in electric field at the interphase and a band bending in the $MnFe_2O_4$ component.

The flat band potential was evaluated by Mott–Schottky curves in a 1 M KOH electrolyte. As shown in Figure S5, the flat band potentials of $Ni/MnFe_2O_4$ are around 1.26 V vs. RHE higher than that of $MnFe_2O_4$ at 1.19 V vs. RHE, thus, facilitating the charge transfer between the KOH electrolyte and $Ni/MnFe_2O_4$ electrode. Moreover, the charge carrier concentration increases from 1.7×10^{18} cm^{-3} for $MnFe_2O_4$ to 3.6×10^{18} cm^{-3} for $Ni_{10\%}/MnFe_2O_4$ and continues increasing with the content of Ni to 9.1×10^{20} cm^{-3} for $Ni_{50\%}/MnFe_2O_4$ (Figure S6).

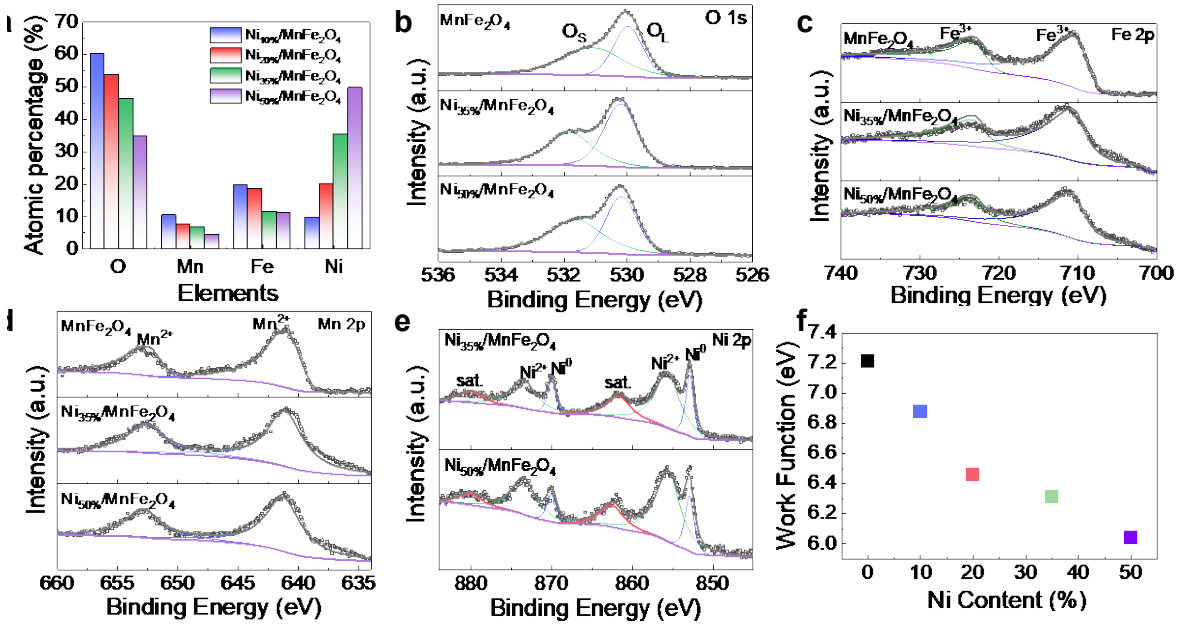

Figure 2. (a) Atomic percentage of O, Mn, Fe, and Ni as obtained by EDS. (b-e) High-resolution O 1s (b), Fe 2p (c), Mn 2p (d), and Ni 2p (e) XPS spectra of $MnFe_2O_4$, $Ni_{35\%}/MnFe_2O_4$ and $Ni_{50\%}/MnFe_2O_4$. (f) Work function of $MnFe_2O_4$, and $Ni/MnFe_2O_4$ with different Ni loadings.

The activity of $Ni/MnFe_2O_4$ catalysts with different Ni loadings toward the OER was evaluated and compared with that of a commercial RuO_2 reference. **Figure 3a** displays the LSV curves and **Figure 3b** shows the overpotential at a current density of 10 mA/cm^2. The overpotential

of $Ni/MnFe_2O_4$ initially decreases and then increases with the Ni loading. $Ni_{35\%}/MnFe_2O_4$ exhibited the lowest overpotential at 261 mV (10 mA/cm^2), significantly below that of $MnFe_2O_4$ (440 mV) and the reference RuO_2 catalysts (333 mV). The Tafel slopes of $Ni/MnFe_2O_4$ show a similar trend as the overpotential, first increasing and then decreasing with the Ni loading. $Ni_{35\%}/MnFe_2O_4$ has the smallest Tafel value of 38.3 mV/dec compared to $MnFe_2O_4$ (87.9 mV/dec) and commercial RuO_2 (72.6 mV/dec), indicating faster kinetics (**Figure 3c**). Overall, the OER performance of $Ni/MnFe_2O_4$ was significantly enhanced compared to $MnFe_2O_4$, Ni, and $Ni(OH)_2$ (Figures S7-S9).

The double-layer capacitance (C_{dl}), which is proportional to the electrochemical active surface area (ECSA), was calculated using cyclic voltammetry (CV) curves (Figure S10). As shown in **Figure 3d,** the C_{dl} value first increased and then decreased with the Ni loading. Among the tested electrocatalysts, $Ni_{35\%}/MnFe_2O_4$ exhibited the largest C_{dl} value at 8.21 mF/cm^2, which is 23 times larger than that of $MnFe_2O_4$ (0.36 mF/cm^2). ECSA values were calculated from C_{dl} and are shown in **Figure 3e**.

Electrochemical impedance spectroscopy (EIS) analyses showed that $Ni_{35\%}/MnFe_2O_4$ exhibited the smallest charge transfer resistance, consistent with its fastest reaction kinetics (**Figure 3f** and Table S1). In comparison to the reference materials tested here and previously reported catalysts, $Ni_{35\%}/MnFe_2O_4$ displayed outstanding OER performance as displayed in **Figure 3g** and Table S2.

The long-term durability of $Ni_{35\%}/MnFe_2O_4$ was subsequently evaluated using chronoamperometry at 1.5 V vs. RHE. As shown in **Figure 3h**, $Ni_{35\%}/MnFe_2O_4$ exhibited durable long-term stability with a minor current density decrease of ca. 5% after 90 h measurement.

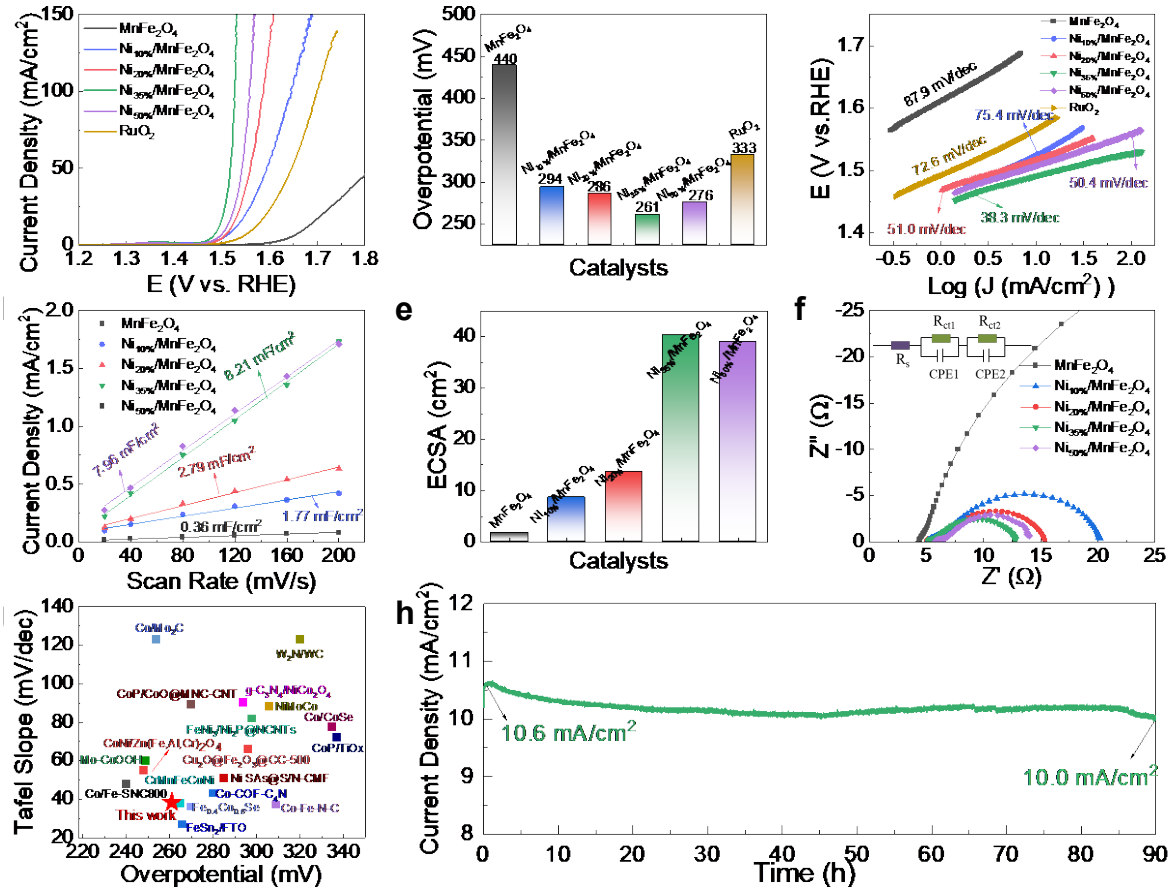

Figure 3. OER performance. (a) LSV curves with the scan rate of 5 mV/s, (b) overpotential at the current density of 10 mA/cm^2, and (c) Tafel slopes of $MnFe_2O_4$, Ni/$MnFe_2O_4$ with different Ni loadings, and commercial RuO_2. (d) C_{dl} values obtained from CV curves, and (e) corresponding the ECSA values of Ni/$MnFe_2O_4$ with different Ni loadings. (f) EIS spectra of Ni/$MnFe_2O_4$ with different Ni loadings. The inset shows the equivalent circuit model used to fit the data. (g) OER comparison between $Ni_{35\%}/MnFe_2O_4$ and recently reported catalysts. (h) Chronoamperometry test of $Ni_{35\%}/MnFe_2O_4$ at 1.50 V vs. RHE.

In situ Raman spectroscopy was used to investigate the surface reconstruction during OER. As shown in Figure S11, a wide peak at around 650 cm^{-1} was observed at 1.1 V vs. RHE, which was indexed as the A_{1g} mode of $MnFe_2O_4$. At a higher potential, NiOH at ~310 cm^{-1}, NiOOH at ~481 cm^{-1}, FeOOH at ~476 and 678 cm^{-1}, and MnOOH at ~625 cm^{-1} were detected, implying the restructuration of the whole Ni/$MnFe_2O_4$ composite material. All the metals were observed to bind

with the key OER intermediate, *OOH. Additionally, we observed the intensity of the Raman peaks associated with the metal oxyhydroxide species to increase with the applied potential, indicating that all of them can act as active OER intermediates. Overall, *in situ* Raman spectroscopy showed the Ni/$MnFe_2O_4$ to reconstruct to NiOOH/MnFeOOH during OER.

HRTEM images of the sample after the long-term stability test did not show obvious lattice fingerprints but the FFT pattern could be indexed to a polycrystalline iron manganese oxide (Figure S12). The XRD pattern after the stability test shows several weak diffraction peaks that match the $MnFe_2O_4$ phase (Figure S13). No additional crystalline secondary phase was detected.

XPS analysis of Ni/$MnFe_2O_4$ after the stability test was employed to gain an understanding of the evolution of the catalysts during OER. As shown in Figure S14a, three O 1s peaks, located at 535.92, 531.8, and 530.23 eV, were obtained. They were indexed to the adsorbed water molecules O_{H_2O}, O_s, and O_L, respectively. The Mn 2p binding energy was 641.64 eV for Mn $2p_{3/2}$, indicating a Mn^{3+} state (Figure S14b). As shown in Figure S14c, the Ni XPS spectrum only shows a doublet at 855.82 eV (Ni $2p_{3/2}$) accompanied by two satellite peaks, which could be indexed to a Ni^{3+} environment. The Fe 2p XPS spectrum displays a doublet at 710.34 eV (Fe $2p_{3/2}$), which is assigned to Fe^{3+}. (Figure S14d). The higher valence of metal ions obtained after the OER stability test is consistent with the surface reconstruction of the material to an oxyhydroxide chemical environment.

DFT calculations were used to gain insight into the OER mechanism in the reconstructed NiOOH/MnFeOOH, MnFeOOH, and NiOOH surfaces. The optimized models are shown in Figures S15-17. The calculated partial density of states (PDOS) shows the d band center of Ni to be at 0.95 eV for NiOOH and 0.87 eV for NiOOH/MnFeOOH. This shift of the d band center of Ni in NiOOH/MnFeOOH compared with NiOOH is related to the charge redistribution taking

place at the interface (Figure S18). This shift indicates NiOOH/MnFeOOH is more favorable to absorb oxygen intermediates (**Figure 4a**). Indeed, the O p orbital from O* displays a stronger overlap with Ni d orbital in NiOOH/MnFeOOH around the Fermi level than that of NiOOH, implying efficient p-d orbital coupling between NiOOH/MnFeOOH and O*. The spin polarization, i.e. the difference in spin-up and spin-down electrons, of O* absorbed on NiOOH/MnFeOOH and NiOOH is calculated to be 0.633 μ_B and 0.652 μ_B (**Figure 4b, 4c**). This difference in spin polarization is related to the spin state of the bonded Ni active sites. The magnetic moment per Ni is calculated to be 0.2394 μ_B for NiOOH/MnFeOOH and 0.1225 μ_B for NiOOH, primarily influenced by the electron spin state. The spin polarization of Ni was further calculated to be 0.310 for NiOOH and 0.613 for NiOOH/MnFeOOH (**Figure 4b, 4c**). Therefore, Ni in NiOOH/MnFeOOH has a relatively higher spin state than Ni in NiOOH.

The Ni 3d PDOS of NiOOH/MnFeOOH reveals a more asymmetric arrangement compared with NiOOH of each d-splitting orbitals channel, signifying the higher spin polarization (Figures S19-20). Based on the crystal field theory and d-orbital splitting manner, 3d orbitals of Ni split into five states: d_{x2-y2}, d_{z2}, d_{xz}, d_{yz}, and d_{xy}, where d_{x2-y2} and d_{z2} states are in twofold orbital degeneracy (*eg*), d_{xz}, d_{yz}, and d_{xy} states are in threefold degeneracy (*t2g*). As shown in **Figure 4d**, 22% and 2% of electrons in the d_{z2} and d_{x2-y2} orbitals are unpaired, while 8%, 5%, and 8% of electrons in d_{yz}, d_{xz} and d_{xy} orbitals are unpaired in NiOOH, while 23% and 5% unpaired electrons are in the d_{z2} and d_{x2-y2} orbitals, 11%, 10%, and 9% unpaired electrons are in the d_{yz}, d_{xz} and d_{xy} orbitals, respectively, for NiOOH/MnFeOOH. Therefore, the probability of the Ni^{3+} in $t2g^5eg^2$ high spin state configuration for NiOOH/MnFeOOH is 5%, which is higher than that of the NiOOH (2%). Unpaired electrons in *eg* and *t2g* can hybridize with O* to form octahedral σ-antibonding *eg* orbitals or π-bonding *t2g* orbitals. Since it requires higher energy to form the antibonding orbital,

Ni^{3+} in high spin state can decrease the bond energy barrier with O*, leading to a lower overpotential. Besides, the orbital occupancy number can influence the adsorption ability of OH^-, O_2, and oxygen intermediates[22], thus modulating the reaction kinetics process. Figure S21 shows the crystal orbital Hamilton population (COHP) of Ni-O bond analysis. The length of the Ni-O bond between NiOOH/MnFeOOH and O* is 1.97 Å, lower than that of 2.02 Å for NiOOH, providing a stronger bond strength with O*.

Because the lowest energy state of the oxygen molecule is a paramagnetic triplet state, the formation of oxygen from OH^- in a diamagnetic singlet state is favored when both adsorbed O molecules have aligned spins[17a, 18c, 23]. The higher spin-polarization of Ni within NiOOH/MnFeOOH compared with Ni within NiOOH can favor a higher degree of parallel spin alignment of the oxygen intermediates. The spin orbit interactions between Ni and the OER intermediates are shown in **Figure 4f**. For Ni in a high spin state, the first step is the adsorption of OH- at the Ni active sites to form the intermediate of HO(↓)*. Then, the electron transfers at the surface to generate O(↓)* species followed by the formation of triplet state intermediate HO(↓)O(↓)*. Last, the HO(↓)O(↓)* is transferred into O_2. Due to the higher spin state of Ni in NiOOH/MnFeOOH, the oxygen radicals tend to align in parallel to promote the O-O bond formation within relatively low energy, which is a common phenomenon in ferromagnetic catalysts under an external magnetic field[24]. The hybridization of the Ni 3d orbit from a high spin Ni and O 2p orbit from the oxygen intermediates will facilitate spin-selected charge transport and optimize the kinetics of the spin-charge transfer. Meanwhile, the spin polarization of O will occur with fast kinetics under the principle of spin angular momentum conservation.[17a] However, the low spin-polarization of Ni led to a random spin distribution of O in HOO*, resulting in both HO(↓)O(↓)* and HO(↓)O(↑)* distribution. The latter oxygen configuration requires extra energy to

achieve the oxygen spin flip, leading to a higher overpotential to form the triplet state O_2, otherwise, it directly forms the singlet state O_2 by requiring extra energy. Regardless of both processes, the non-parallel spin arrangement requires additional energy to produce O_2.

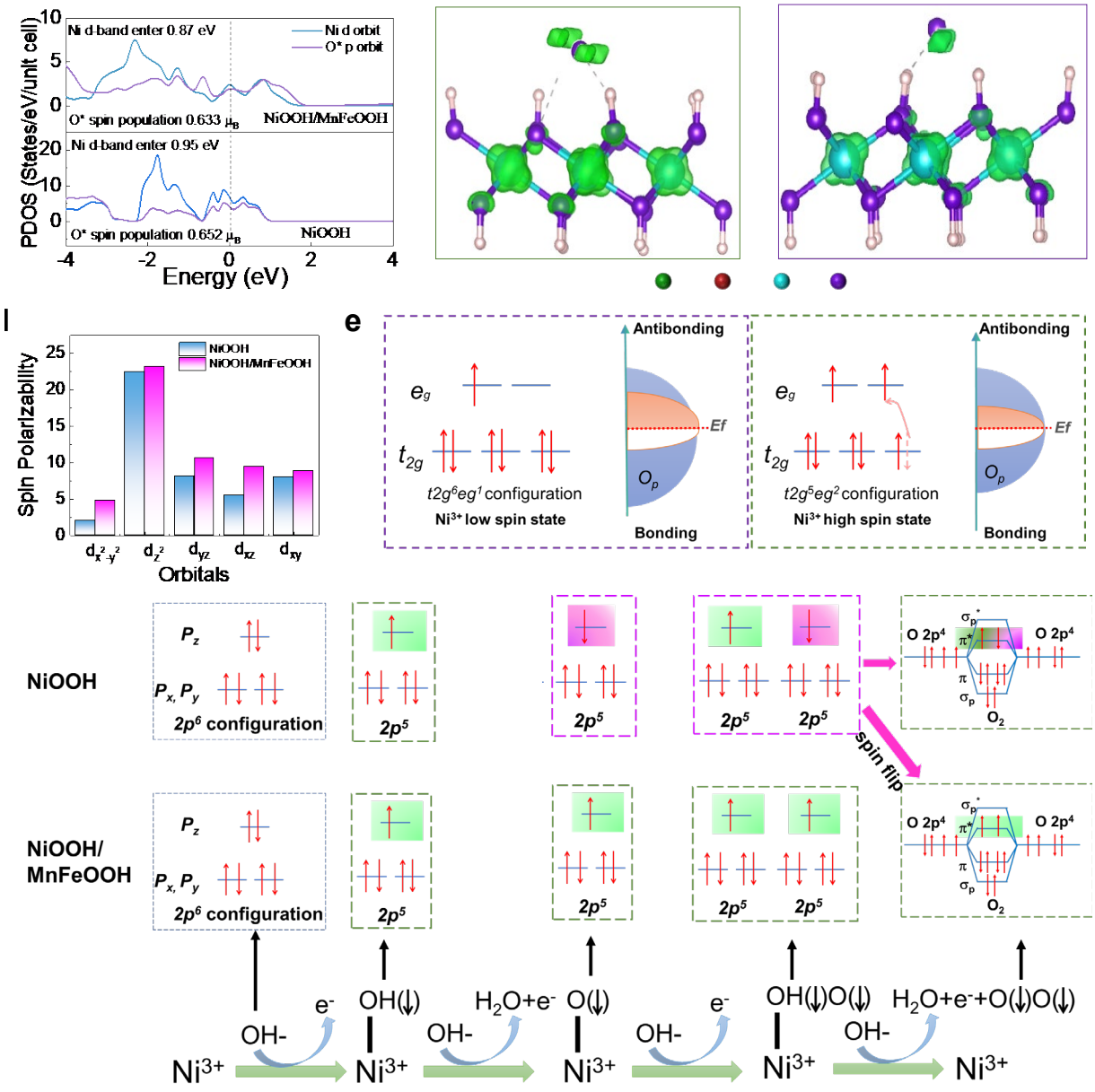

Figure 4. (a) PDOSs curves of NiOOH/MnFeOOH and NiOOH structures. (b, c) Spin polarization difference diagram of NiOOH/MnFeOOH (b) and NiOOH (c). The contour around the atoms

represents spin-up electrons (green). (d) The spin polarizability calculation of splitting orbitals of both NiOOH/MnFeOOH and NiOOH. (e) Illustration of the Ni^{3+} electron configuration of NiOOH/MnFeOOH with a high spin state and NiOOH with a low spin state. (f) The OER process with and without the spin-aligned process in NiOOH/MnFeOOH and NiOOH.

For the OER process, the first step is the OH^- adsorption and the last step is the O_2 release from the catalyst surface. Therefore, the OH^- and O_2 adsorption energy in different active sites was considered in the different reconstructed catalysts. As shown in **Figure 5a**, the Ni atoms on the NiOOH/MnFeOOH surface show larger absolute adsorption energy of OH^- than Fe and Mn atoms. Besides, the Ni/Fe/Mn sites in the NiOOH/MnFeOOH heterojunction are characterized by higher OH^- adsorption energies than their counterparts of NiOOH and MnFeOOH. The calculated difference in adsorption energy at Ni/Fe/Mn sites in NiOOH/MnFeOOH compared with NiOOH and MnFeOOH is related to the different spin polarization differences (**Figures 4b,c**) and the charge redistribution taking place at the interface (Figure S18). The adsorption energy of O_2 at Fe/Mn/Ni active sites on the NiOOH/MnFeOOH surface is positive, implying that O_2 is easy to release from the surface of the catalysts (**Figure 5b**). Among them, the Ni active sites are the ones showing the highest positive adsorption energies. Besides, Ni/Fe/Mn active sites on the NiOOH/MnFeOOH heterostructure show higher positive O_2 adsorption energies than on NiOOH and MnFeOOH thus facilitating the O_2 release, freeing the surface site for the subsequent reactions.

From a thermodynamic perspective, the Gibbs free energies were calculated to reveal the energy barriers of adsorption/desorption of key intermediates. The step diagram of the OER process with an applied energy of 0 V and 1.23 V is shown in **Figure 5c** and the models of oxygen intermediates adsorbed on the NiOOH/MnFeOOH are shown in Figure S22. **The** NiOOH/MnFeOOH structure displays a smaller energy barrier of the potential determining step (PDS) than NiOOH, with a calculated overpotential of 0.29 eV compared to the 0.38 eV obtained

for NiOOH (**Figure 5c, d**). The smaller energy barrier is attributed to the spin state modulation of both the Ni active sites and the oxygen intermediates.

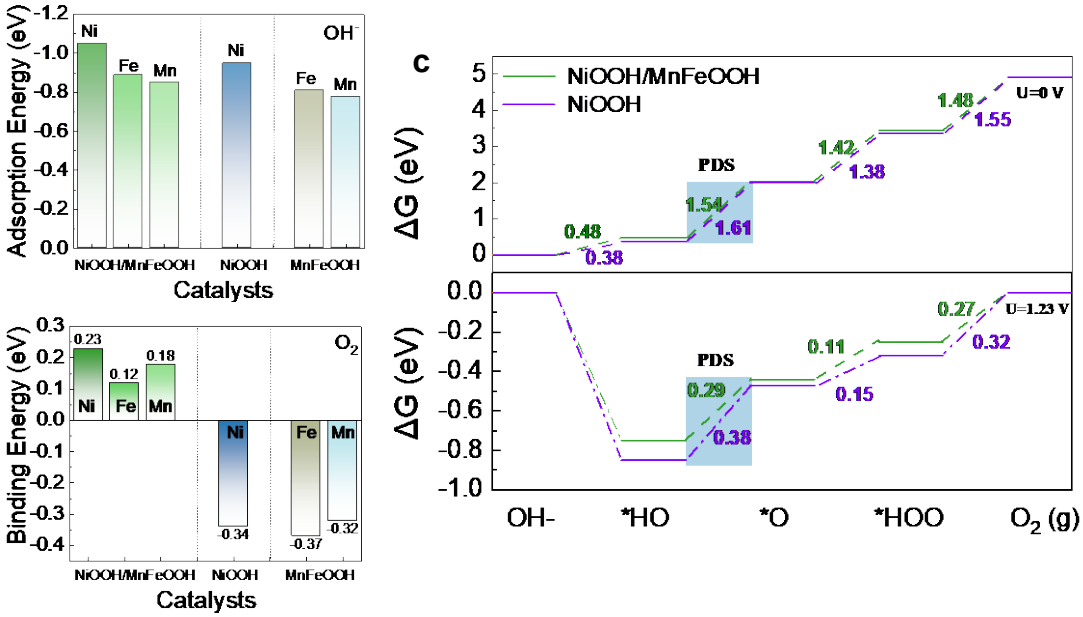

Figure 5. (a) OH^- and (b) O_2 adsorption energy for different active sites in different structures of NiOOH/MnFeOOH, NiOOH, and MnFeOOH. (c) Free energy step diagram during of the OER process at an applied voltage of 0 V (up) and 1.23 V (down).

To evaluate the performance of NiOOH/MnFeOOH derived from $Ni_{35\%}/MnFe_2O_4$ as a bifunctional oxygen electrocatalyst, oxygen reduction reaction (ORR) measurements were performed in 0.1 M KOH using a rotating ring disk electrode (RRDE, see details in the SI). A commercial Pt/C sample was also tested as a reference. Figure S23a shows the CV curves measured from NiOOH/MnFeOOH both in Ar and O_2 saturated electrolytes. Compared with the CV curves within an Ar-saturated electrolyte showing no obvious electrochemical feature for the NiOOH/MnFeOOH, a noticeable cathodic peak was observed when NiOOH/MnFeOOH was used in O_2-saturated electrolyte, indicating good electrocatalytic activity toward ORR. Figure S23b shows the ORR CV curves within Ar and O_2-saturated electrolyte of commercial Pt/C. The LSV curves obtained from the NiOOH/MnFeOOH and Pt/C catalysts at different rotation speeds in the

range from 400 rpm to 2500 rpm are shown in Figure S24. Figure S25 shows the LSV curves of the catalysts at the rotation speed of 1600 rpm. NiOOH/MnFeOOH shows a similar limiting current density as Pt/C. The potential gap (E_{gap}) between the overpotential for OER and the half-wave potential for ORR of NiOOH/MnFeOOH is calculated to be 0.72 V, which is comparable to that of Pt/C+RuO_2 (0.73 V, Figure S26).

Reversible aqueous ZABs were assembled using a NiOOH/MnFeOOH–based air cathode (see details in the SI). ZABs based on 20 wt% Pt/C mixed with RuO_2 (Pt/C+RuO_2) were also assembled and tested as a reference. The ZABs based on a NiOOH/MnFeOOH cathode exhibit an open-circuit potential (OCP) of 1.56 V, i.e. 94 % of its theoretical limit (1.66 V),[25] slightly above that of the Pt/C+RuO_2-based ZABs (1.50 V) (**Figure 6a**). As shown in Figure S27, the assembled ZABs could light a LED sign with a required input voltage of 1.4 V. At a current density of 8 mA/cm^2, the NiOOH/MnFeOOH-based ZAB delivered a specific capacity of 814 mAh g^{-1}, slightly above that of the Pt/C+RuO_2-based ZAB, 793 mAh g^{-1} (**Figure 6b**). Besides, the peak power density of the NiOOH/MnFeOOH-based ZAB was 120 mW/cm^2, also above that of the Pt/C+RuO_2-based ZAB at 112 mW/cm^2 (**Figure 6c**). Most importantly, as shown in **Figure 6d**, the NiOOH/MnFeOOH-based ZAB is not only characterized by a lower charge−discharge overpotential, i.e. a higher energy efficiency, compared with the Pt/C+RuO_2-based ZAB, but also much higher durability. The Pt/C+RuO_2-based ZAB shows an obvious overpotential increase after 150 h (450 cycles) of charging/discharging cycles at a current density of 8 mA/cm^2. In contrast, the NiOOH/MnFeOOH-based ZAB exhibits much lower potential variation even after 360 h, i.e. 15 days, (1080 cycles) of continuous charge/discharge operation. More in detail, the charge/discharge potential gap of NiOOH/MnFeOOH-based ZAB is 1.09 V for the first cycle and it slightly increased to 1.14, 1.16, 1.19, 1.23, and 1.26 V for the 200th, 400th, 600th, 800th, and 1000th

cycle, respectively (**Figure 6e**). Overall, the NiOOH/MnFeOOH as the ZAB cathode displays exceptional OCP, specific capacity, and long-term cycling performance when compared with previous published results (Table S3).

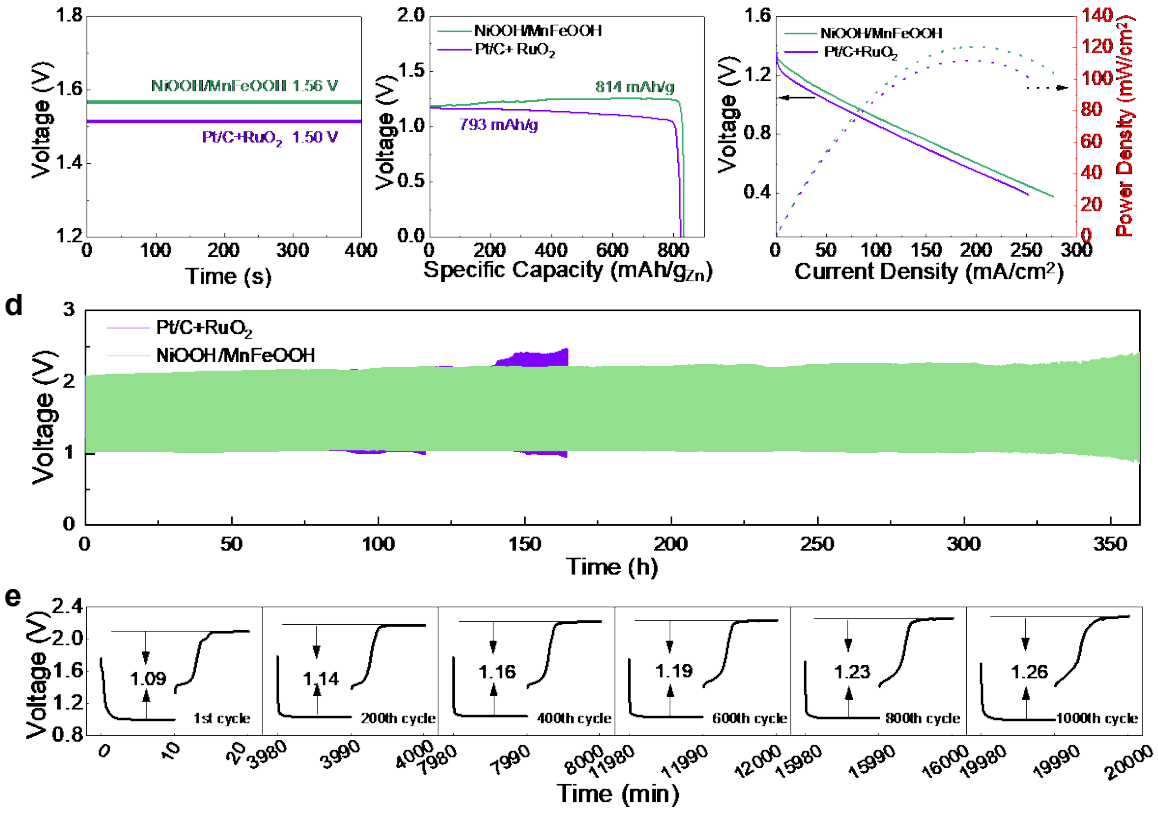

Figure 6. (a) Open circuit potential, (b) specific capacity, and (c) power density of a NiOOH/MnFeOOH-based and a Pt/C+RuO_2-based ZAB. (d) Galvanostatic discharge-charge curves with 10 min discharge and 10 min charge cycles at a current density of 8 mA/cm^2 for a NiOOH/MnFeOOH-based and a Pt/C+RuO_2-based ZAB. (e) Charge/discharge curves at the 1^{st}, 200^{th}, 400^{th},600^{th}, 800^{th} and 1000^{th} cycle for a NiOOH/MnFeOOH-based ZAB.

3. Conclusion

Ni/$MnFe_2O_4$ heterostructured nanoparticles were produced by a simple two-step method. They were characterized by some extent of electron transfer from Ni to $MnFe_2O_4$ at the interphase according to XPS and UPS measurements. *In situ* Raman and XPS spectra demonstrate that the Ni/$MnFe_2O_4$ surface is restructured to NiOOH/MnFeOOH during the OER. NiOOH/MnFeOOH

exhibits excellent OER catalytic performance with an overpotential of 261 mV at 10 mA/cm^2 and a low Tafel slope of 38.3 mV/dec. The larger magnetic moment and the charge redistribution within NiOOH/MnFeOOH as well as the modified spin polarization of adsorbed oxygen intermediates facilitate spin-selected charge transfer by reducing the energy barriers of formation of oxygen molecules. Besides, NiOOH/MnFeOOH shows good bifunctional oxygen properties with notable ORR performance. Thus, NiOOH/MnFeOOH is used as an air cathode in rechargeable aqueous ZABs, showing a high OCP value of 1.56 V, a high specific capacity of 814 mAh g^{-1}, and a 360 h (over 1000 cycles) long-term stability. This study provides insight into spin polarization modulation of both metal active sites and oxygen intermediates adjusted by constructing a heterojunction without applying an external magnetic field to boost the OER performance.

Supporting Information

Supporting Information is available from the Wiley Online Library or from the author.

Acknowledgements

L. Yang and R. H contributed equally to this work. L. Yang thanks the China Scholarship Council (CSC) for the scholarship support (202008130132). ICN2 acknowledges funding from Generalitat de Catalunya 2021SGR00457. This study is part of the Advanced Materials programme and was supported by MCIN with funding from European Union NextGenerationEU (PRTR-C17.I1) and by Generalitat de Catalunya. The authors thank support from the project NANOGEN (PID2020-116093RB-C43), funded by MCIN/ AEI/10.13039/501100011033/ and by "ERDF A way of making Europe", by the "European Union". ICN2 is supported by the Severo Ochoa program from Spanish MCIN / AEI (Grant No.: CEX2021-001214-S) and is funded by the CERCA Programme / Generalitat de Catalunya. Part of the present work has been performed in the framework of

Universitat Autònoma de Barcelona Materials Science PhD program. M.B. acknowledges support from SUR Generalitat de Catalunya and the EU Social Fund; project ref. 2020 FI 00103. ICN2 is founding member of e-DREAM.[X]

Declaration of Competing Interest

There are no conflicts to declare.

Data Availability Statement

The data that support the findings of this study are available from the corresponding author upon reasonable request.

References.

[1] a)D. Larcher, J. M. Tarascon, *Nat. Chem.* **2015**, 7, 19; b)J. Lv, J. Xie, A. G. A. Mohamed, X. Zhang, Y. Wang, *Chem. Soc. Rev.* **2022**, 51, 1511; c)Y. Zhai, B. Zhang, R. Shi, S. Zhang, Y. Liu, B. Wang, K. Zhang, G. I. N. Waterhouse, T. Zhang, S. Lu, *Adv. Energy Mater.* **2021**, 12, 2103426; d)K. Wang, H. Li, G. Guo, L. Zheng, S. Passerini, H. Zhang, *ACS Energy Lett.* **2023**, 8, 1671; e)J. Li, L. Li, X. Ma, X. Han, C. Xing, X. Qi, R. He, J. Arbiol, H. Pan, J. Zhao, J. Deng, Y. Zhang, Y. Yang, A. Cabot, *Adv. Sci.***2023**, 10, e2300841.

[2] a)R. He, L. Yang, Y. Zhang, X. Wang, S. Lee, T. Zhang, L. Li, Z. Liang, J. Chen, J. Li, A. O. Moghaddam, J. Llorca, M. Ibanez, J. Arbiol, Y. Xu, A. Cabot, *Energy Stor. Mater.* **2023**, 58, 287; b)Q. Wang, Q. Feng, Y. Lei, S. Tang, L. Xu, Y. Xiong, G. Fang, Y. Wang, P. Yang, J. Liu, W. Liu, X. Xiong, *Nat. Commun.* **2022**, 13, 3689; c)T. Zhou, N. Zhang, C. Wu, Y. Xie, *Energy & Environ. Sci.* **2020**, 13, 1132.

[3] a)D. Chen, J. Zhu, X. Mu, R. Cheng, W. Li, S. Liu, Z. Pu, C. Lin, S. Mu, *Appl. Catal. B-Environ.* **2020**, 268, 118729; b)W. Cheng, P. Yuan, Z. Lv, Y. Guo, Y. Qiao, X. Xue, X. Liu, W. Bai, K. Wang, Q. Xu, J. Zhang, *Appl. Catal. B-Environ.* **2020**, 260, 118198; c)J. Abed, S. Ahmadi, L. Laverdure, A. Abdellah, C. P. O'Brien, K. Cole, P. Sobrinho, D. Sinton, D. Higgins, N. J. Mosey, S. J. Thorpe, E. H. Sargent, *Adv. Mater.* **2021**, 33, e2103812; d)C. He, L. Yang, X. Peng, S. Liu, J. Wang, C. Dong, D. Du, L. Li, L. Bu, X. Huang, *ACS Nano* **2023**, 17, 5861.

[4] M. Yu, E. Budiyanto, H. Tuysuz, *Angew Chem Int. Ed.* **2022**, 61, e202103824.

[5] a)X. Wang, X. Han, R. Du, Z. Liang, Y. Zuo, P. Guardia, J. Li, J. Llorca, J. Arbiol, R. Zheng, A. Cabot, *Appl. Catal. B-Environ.* **2023**, 320, 121988; b)X. Wang, J. Li, Q. Xue, X. Han, C. Xing, Z. Liang, P. Guardia, Y. Zuo, R. Du, L. Balcells, J. Arbiol, J. Llorca, X. Qi, A. Cabot, *ACS Nano* **2023**, 17, 825; c)M. Li, S. Wang, X. Wang, X. Tian, X. Wu, Y. Zhou, G. Hu, L. Feng, *Chem. Eng. J.* **2022**, 442, 136165.

[6] Y. Cheng, S. Dou, J. P. Veder, S. Wang, M. Saunders, S. P. Jiang, *ACS Appl. Mater. Interfaces* **2017**, 9, 8121.

[7] a)M. Liu, Z. Zhao, X. Duan, Y. Huang, *Adv. Mater.* **2019**, 31, e1802234; b)X. Wang, Z. Li, Y. Qu, T. Yuan, W. Wang, Y. Wu, Y. Li, *Chem* **2019**, 5, 1486.

[8] a)J. Zhang, J. Lian, Q. Jiang, G. Wang, *Chem. Eng. J.* **2022**, 439, 135502; b)Y. Li, S. H. Talib, D. Liu, K. Zong, A. Saad, Z. Song, J. Zhao, W. Liu, F. Liu, Q. Ji, P. Tsiakaras, X. Cai, *Appl. Catal. B-Environ.* **2023**, 320, 122023; c)J. Ran, L. Wang, M. Si, X. Liang, D. Gao, *Small* **2023**, 19, e2206367.

[9] a)Z. Liang, T. Zhang, P. Cao, T. Yoshida, W. Tang, X. Wang, Y. Zuo, P. Tang, M. Heggen, R. E. Dunin-Borkowski, J. R. Morante, A. Cabot, M. Yamashita, J. Arbiol, *Chem. Eng. J.* **2022**, 442, 136129; b)Z. Liang, J. Wang, P. Tang, W. Tang, L. Liu, M. Shakouri, X. Wang, J. Llorca, S.

Zhao, M. Heggen, R. E. Dunin-Borkowski, A. Cabot, H. B. Wu, J. Arbiol, *Appl. Catal. B-Environ.* **2022**, 314, 121451; c)C. Lai, H. Li, Y. Sheng, M. Zhou, W. Wang, M. Gong, K. Wang, K. Jiang, *Adv. Sci.* **2022**, 9, e2105925; d)R. Gan, Y. Song, C. Ma, J. Shi, *Appl. Catal. B-Environ.* **2023**, 327, 122443.

[10] a)L. Zhang, W. Wang, S. Sun, D. Jiang, E. Gao, *Appl. Catal. B-Environ.* **2015**, 162, 470; b)Y. Zhang, F. Ding, C. Deng, S. Zhen, X. Li, Y. Xue, Y.-M. Yan, K. Sun, *Catal. Commun.* **2015**, 67, 78.

[11] a)B. Zheng, J. Duan, Q. Tang, *Dalton Trans* **2022**, 51, 7491; b)Y. Li, Y. Zhang, K. Qian, W. Huang, *ACS Catal.* **2022**, 12, 1268; c)K. Qian, H. Duan, Y. Li, W. Huang, *Chemistry* **2020**, 26, 13538; d)H. Zhang, Y. Zhou, M. Xu, A. Chen, Z. Ni, O. Akdim, T. Wågberg, X. Huang, G. J. A. n. Hu, *ACS Nano* **2022**, 17, 636; e)P. Sun, Y. Zhou, H. Li, H. Zhang, L. Feng, Q. Cao, S. Liu, T. Wågberg, G. Hu, *Appl. Catal. B-Environ.* **2022**, 310, 121354.

[12] a)Y. Kang, S. Wang, K. S. Hui, S. Wu, D. A. Dinh, X. Fan, F. Bin, F. Chen, J. Geng, W.-C. M. Cheong, K. N. Hui, *Nano Res.* **2021**, 15, 2952; b)B.-Y. Shi, C.-B. Yao, H.-Y. Li, H.-X. Cao, X.-Y. Zheng, Y. Liu, H.-T. Yin, *ACS Appl. Nano Mater.* **2023**, 6, 2972; c)D. Li, H. Liu, H. Liu, Y. Chen, C. Wang, L. Guo, *Dalton Trans.* **2023**, 52, 5192; d)Y. Dang, G. Wang, G. Su, Z. Lu, Y. Wang, T. Liu, X. Pu, X. Wang, C. Wu, C. Song, Q. Zhao, H. Rao, M. Sun, *ACS Nano* **2022**, 16, 4536; e)H. Chen, K. Jie, C. J. Jafta, Z. Yang, S. Yao, M. Liu, Z. Zhang, J. Liu, M. Chi, J. Fu, S. Dai, *Appl. Catal. B-Environ.* **2020**, 276, 119155.

[13] a)H. W. Go, T. T. Nguyen, Q. P. Ngo, R. Chu, N. H. Kim, J. H. Lee, *Small* **2023**, 19, e2206341; b)W. Li, L. Wu, X. Wu, C. Shi, Y. Li, L. Zhang, H. Mi, Q. Zhang, C. He, X. Ren, *Appl. Catal. B-Environ.* **2022**, 303, 120849; c)K. Li, R. Cheng, Q. Xue, P. Meng, T. Zhao, M. Jiang, M. Guo, H.

Li, C. Fu, *Chem. Eng. J.***2022**, 450, 137991; d)C. He, Q. Liu, H. Wang, C. Xia, F. M. Li, W. Guo, B. Y. Xia, *Small* **2023**, e2207474.

[14] Y. Niu, X. Teng, S. Gong, X. Liu, M. Xu, Z. Chen, *Energy Stor. Mater.* **2021**, 43, 42.

[15] Q. Dong, H. Wang, J. Ren, X. Wang, R. Wang, *Chem. Eng. J.* **2022**, 442, 136128.

[16] X. Liu, W. Liu, M. Ko, M. Park, M. G. Kim, P. Oh, S. Chae, S. Park, A. Casimir, G. Wu, J. Cho, *Adv. Funct. Mater.* **2015**, 25, 5799.

[17] a)X. Ren, T. Wu, Y. Sun, Y. Li, G. Xian, X. Liu, C. Shen, J. Gracia, H. J. Gao, H. Yang, Z. J. Xu, *Nat. Commun.* **2021**, 12, 2608; b)G. Shen, R. Zhang, L. Pan, F. Hou, Y. Zhao, Z. Shen, W. Mi, C. Shi, Q. Wang, X. Zhang, J. J. Zou, *Angew Chem. Int. Ed.* **2020**, 59, 2313.

[18] a)Y. Miao, Q. Huang, D. Wen, D. Xie, B. Huang, D. Lin, C. Xu, W. Zeng, F. Xie, *RSC Adv.* **2023**, 13, 4249; b)Y. Sun, S. Sun, H. Yang, S. Xi, J. Gracia, Z. J. Xu, *Adv. Mater.* **2020**, 32, e2003297; c)S. Jiang, F. Chen, L. Zhu, Z. Yang, Y. Lin, Q. Xu, Y. Wang, *ACS Appl. Mater. Interfaces* **2022**, 14, 10227.

[19] F. A. Garcés-Pineda, M. Blasco-Ahicart, D. Nieto-Castro, N. López, J. R. Galán-Mascarós, *Nature Energy* **2019**, 4, 519.

[20] Y. Sun, J. Wang, Q. Liu, M. Xia, Y. Tang, F. Gao, Y. Hou, J. Tse, Y. Zhao, *J. Mater. Chem. A* **2019**, 7, 27175.

[21] B. Ghosh, *Appl. Surf. Sci.* **2008**, 254, 4908.

[22] a)W. H. Lee, M. H. Han, Y. J. Ko, B. K. Min, K. H. Chae, H. S. Oh, *Nat. Commun.* **2022**, 13, 605; b)J. Wang, L. Li, H. Tian, Y. Zhang, X. Che, G. Li, ACS Appl. Mater. Interfaces **2017**, 9, 7100.

[23] J.-H. Li, J. Wu, Y.-X. Yu, J. Mater. Chem. A **2021**, 9, 10186.

[24] a)J. Ge, R. R. Chen, X. Ren, J. Liu, S. J. H. Ong, Z. J. Xu, Adv. Mater. **2021**, 33, e2101091;

b)J. Yan, Y. Wang, Y. Zhang, S. Xia, J. Yu, B. Ding, Adv. Mater. **2021**, 33, e2007525.

[25] J. Fu, Z. P. Cano, M. G. Park, A. Yu, M. Fowler, Z. Chen, *Adv. Mater.* **2017**, 29, 1604685.